Correlating tau pathology to brain atrophy using a physics-based Bayesian model

Amelie Schäfer[1*†], Pavanjit Chaggar[2†], Alain Goriely[2], Ellen Kuhl[1*] and the Alzheimer's Disease Neuroimaging Initiative[3]

[1]Department of Mechanical Engineering, Stanford University, Stanford,California, USA.

[2]Mathematical Institute, University of Oxford, Oxford, United Kingdom.

[3]Data used in preparation of this article were obtained from the Alzheimer's Disease Neuroimaging Initiative (ADNI) database (adni.loni.usc.edu). As such, the investigators within the ADNI contributed to the design and implementation of ADNI and/or provided data but did not participate in analysis or writing of this report. A complete listing of ADNI investigators can be found at:http://adni.loni.usc.edu/wp-content/uploads/how_to_apply/ADNI_Acknowledgement_List.pdf.

*Corresponding author(s). E-mail(s): amesch@stanford.edu; ekuhl@stanford.edu;

†contributed equally

Abstract

Misfolded tau proteins are a classical hallmark of Alzheimer's disease. Increasing evidence indicates that tau–and not amyloid–is the main agent in driving neurodegeneration and tissue atrophy in Alzheimer's brains. However, the precise correlation between tau and atrophy remains insufficiently understood. Here we explore tau-atrophy interactions by integrating a multiphysics brain network model and longitudinal neuroimaging data for n = 61 subjects from the Alzheimer's Disease Neuroimaging Initiative. Using Bayesian inference with a hierarchical prior structure, we personalize subject-level parameter distributions for each individual subject and infer group-level parameter distributions for amyloid positive and negative groups. Our results show that the group-level tau growth for amyloid positive subjects of 0.0161/year is significantly larger (p=0.0036) than for amyloid negative subjects of

-0.2042/year. Similarly, the group-level tau-induced atrophy for amyloid positive subjects of 0.0165/year is significantly larger (p=0.0048) than for amyloid negative subjects of 0.0111/year. These findings support the hypothesis that amyloid pathology has a magnifying effect on tau pathology and tissue atrophy. Our model may serve as a descriptive tool to quantify the correlation between tau and atrophy, as well as a predictive tool to estimate personalized tau pathology, atrophy, and cognitive impairment timelines from a sequence of medical images.

1 Introduction

Alzheimer's disease is characterized by two proteopathies that take place in patients' brains a decade or more before clinical diagnosis. Plaques of extracellular amyloid-β proteins and neurofibrillary tangles of misfolded tau proteins are typically found upon autopsy of affected brain tissue [1]. Positron emission tomography is currently emerging as a promising, non-invasive technology to visualize and quantify amyloid-β and tau proteins in vivo [2, 3]. While amyloid has long been thought of as the earliest initiator of the pathological cascade in Alzheimer's disease [4], multiple studies now suggest that hyperphosphorylated tau is more closely related to cognitive impairment and propose tau as the major driver of neurodegeneration [5–9].

Macroscopically, the degeneration and loss of neurons manifests itself in a loss of gray matter tissue, thinning of the cortex, widening of cortical sulci, and expansion of the lateral ventricles [10–13]. A multitude of clinical studies have investigated the characteristics of brain atrophy in comparison to healthy aging and longitudinally across advancing stages of Alzheimer's disease. Three main findings are ubiquitous in the literature: brain atrophy rates are higher in Alzheimer's patients than in healthy age-matched controls [14–16], atrophy rates increase over time and with advancing disease [17–20] but may decrease at late disease stages [14, 19, 21], and regional atrophy is strongly related to regional intensity of tau pathology as indicated by autopsy or on tau positron emission tomography images [7, 8, 22]. In fact, tau pathology and cortical atrophy seem to follow the same stereotypical spatiotemporal progression [11, 23–25]: Changes are first observed in the medial temporal lobe, with the hippocampus and entorhinal cortex representing the first affected regions [26]. With advancing disease, an increasing number of neocortical regions are affected by tau neurofibrillary tangles and atrophy, initially the lateral temporal lobe, followed by frontal and parietal lobes. The sensorimotor and visual cortices are typically the only areas spared from tau pathology and atrophy up until late disease stages [24].

Computational models are a promising approach for examining the interplay of different disease mechanisms, like tau pathology and atrophy, in a quantitative manner. Due to the close correlation between tau, atrophy, and the impairment of cognitive function, coupled models of tau and atrophy have

high potential for predicting personalized timelines of disease progression. Several studies have explored computational models for tau pathology, mostly using cross-sectional positron emission tomography or atrophy data for validation [27–29]. We have previously shown that a network reaction-diffusion model for misfolded tau protein can be personalized to individual patient pathologies using Bayesian inference and longitudinal tau positron emission tomography data from 76 subjects [30]. While several mathematical models can qualitatively explain the relationship between tau pathology and atrophy dynamics [31–34], these models have yet to be quantified and validated against longitudinal and multimodal neuroimaging data.

We have recently introduced a coupled tau atrophy model informed by clinical observations of atrophy characteristics and dynamics [35]. We have personalized the model parameters to a preliminary set of longitudinal tau positron emission tomography and structural magnetic resonance images for $n = 4$ subjects and shown that the model predicts realistic atrophy rates that are in line with clinical findings. Our results suggest that the model parameter that characterizes tau-induced atrophy is similar across the entire data set, while other model parameters display notable inter-individual differences. Here we apply the same tau-atrophy model to a cohort of $n = 61$ subjects from the Alzheimer's Disease Neuroimaging Initiative (ADNI) [36] database, of which $n = 38$ subjects have previously been identified as amyloid positive and $n = 23$ as amyloid negative [37]. Clinical diagnoses range from cognitively normal to mild cognitive impairment in both amyloid groups. The expanded cohort allows us to adopt a hierarchical model structure during parameter inference and gain insight into group differences depending on amyloid status. Since amyloid is a known precursor for tau pathology and an indicator for progression to Alzheimer's disease, *we hypothesize that tau and atrophy dynamics differ between amyloid positive and amyloid negative individuals.*

2 Results

2.1 Subject data

Figure 1 illustrates regional misfolded tau concentrations and amounts of atrophy after averaging across all subjects and longitudinal scans in each amyloid group. The processed image data confirm several expected trends: We observe higher tau and atrophy values in the $n = 38$ amyloid positive subjects, who are more likely to be prospective Alzheimer's patients, than in the $n = 23$ amyloid negative subjects. Especially in the amyloid positive group, we also notice a strong topographic relationship between elevated concentrations of misfolded tau and elevated atrophy.

Figure 2 shows the subject-wise trajectory of atrophy over a maximum span of 14 years. Each trajectory starts with an atrophy value of zero at the baseline scan, from which we determine reference regional volumes. When averaging volume changes at follow-up visits globally, across all brain regions, we

observe only a slight overall increase in atrophy over time across amyloid positive subjects, and even less incline across amyloid negative subjects. However, the increase in atrophy over time becomes more apparent when focusing on regions that are known to be affected by atrophy early on in the disease. When averaging atrophy values over the regions of the temporal lobe and the basal ganglia, we observe a pronounced increase in atrophy values, especially across amyloid positive subjects.

Figure 3 summarizes the regionally averaged atrophy rates and highlights differences in atrophy dynamics between regions and amyloid status. The results show notably higher atrophy rates in subjects with positive amyloid status than in those with negative amyloid status, with a significant difference in the hippocampus ($p = 0.015$). The plot also illustrates that the atrophy in our data roughly follows the spatiotemporal evolution described in the literature for tau and atrophy. Atrophy rates are highest in the basal ganglia regions and the temporal lobe, with especially pronounced rates in the hippocampus and entorhinal cortex. Consistent with the pattern of spatiotemporal disease progression, regions of the frontal lobe exhibit lower atrophy rates than temporal regions, closely followed by parietal and occipital regions.

2.2 Posterior distributions

Our model contains three parameters: a transport coefficient ρ characterizing the diffusion of misfolded tau seeds along the connectome, a growth coefficient α characterizing the local production or clearance of misfolded tau protein, and a tau-induced atrophy coefficient G_c quantifying the effect of local tau pathology on local atrophy. Our Bayesian approach for parameter identification results in converged posterior distributions for all three model parameters on the group and subject levels. All hierarchical and individual posteriors have a high effective sample size, $0.99 \leq \hat{r} \leq 1.001$ and significant movement away from the weakly informative priors.

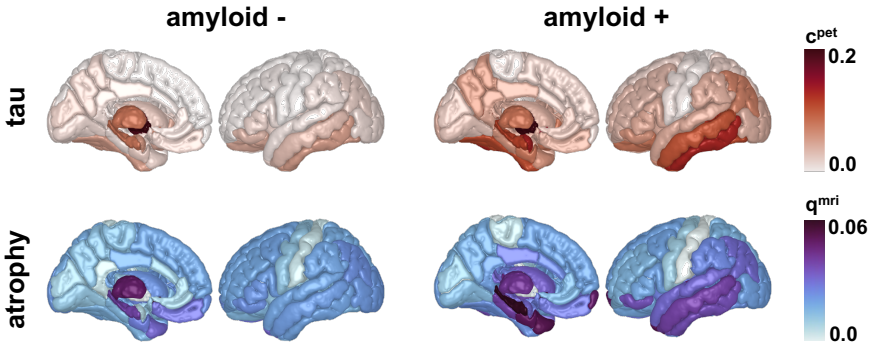

Fig. 1 Imaging data. Regional tau concentrations and atrophy values averaged across all subjects and visits for amyloid positive and negative groups illustrated on a template brain.

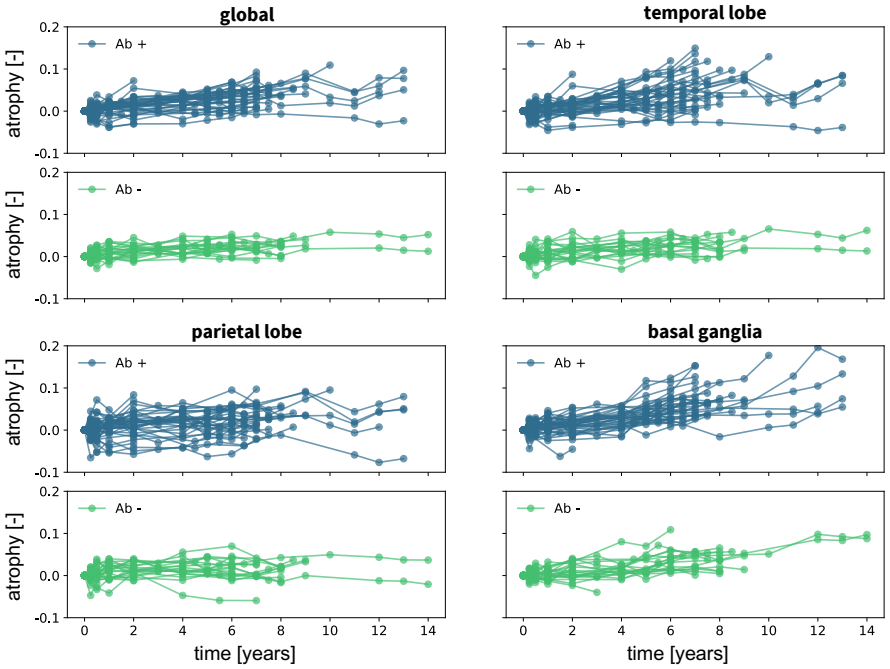

Fig. 2 Atrophy data. Relative atrophy over time shown globally for all brain regions, the temporal lobe, the parietal lobe, and the basal ganglia, for amyloid positive and negative groups.

Figures 4, 5 and 6 and Table 1 summarize the resulting posterior distributions. There are no significant differences in the posterior distributions for the group mean transport coefficient μ^{ρ} between amyloid groups, with both distributions being concentrated close to zero. This similarly is reflected in the likeliness between the profiles of the individual posterior distributions in Figure 4. In contrast, the posterior distributions for the group level growth coefficient μ^{α} exhibit clear differences between amyloid groups. Overall, amyloid positive subjects exhibit a significantly (p =0.0034) higher tau protein growth rate than amyloid negative subjects, with a hyperdistribution mean of 0.017/year and individual distribution means ranging from -0.628/year to 0.444/year for the amyloid positive group, and a hyperdistribution mean of -0.192/year and individual distribution means ranging from -0.742/year to 0.281/year for the amyloid negative group. While the hyperdistributions for the tau-induced atrophy coefficient G_c show much overlap for both amyloid groups, there are noticeably more subjects with higher atrophy coefficients in the amyloid positive group. In fact, a comparison between individual distribution means in an independent t-test shows that atrophy coefficients are significantly higher (p =0.0033) for amyloid positive subjects than for amyloid negative subjects. The average subject-specific noise estimates for tau PET data, $\overline{\sigma}^{\mathrm{s}}_{\mathrm{t}}$, are lower than those for MRI-derived atrophy data, $\overline{\sigma}^{\mathrm{s}}_{\mathrm{a}}$, in both

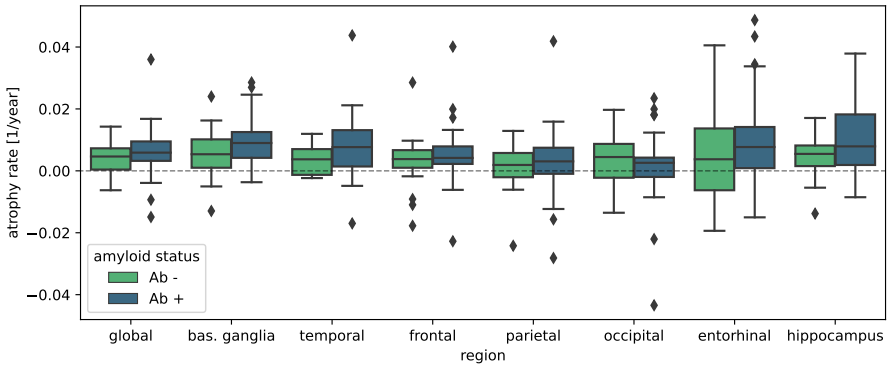

Fig. 3 Atrophy rates. Median atrophy rates between visits separated by regions for amyloid positive and negative groups. Asterisk indicates significant difference between amyloid groups.

amyloid groups: $\overline{\sigma}^{s}_{t} = 0.025$, $\overline{\sigma}^{s}_{a} = 0.043$ for amyloid positive subjects, and $\overline{\sigma}^{s}_{t} = 0.019$, $\overline{\sigma}^{s}_{a} = 0.035$ for amyloid negative subjects.

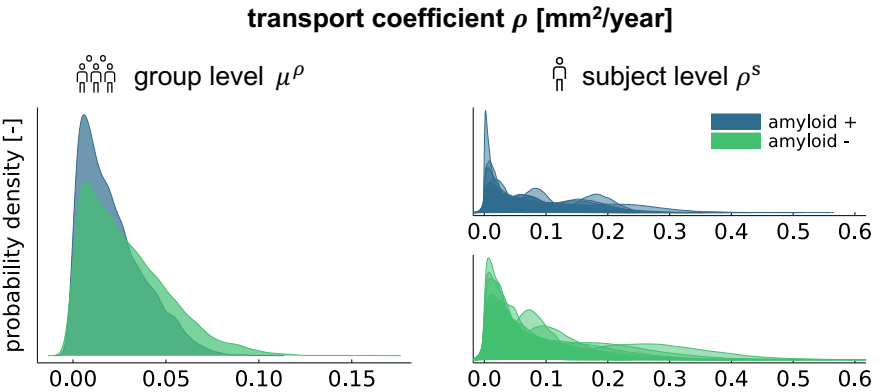

Fig. 4 Posterior distributions. Group- and subject-level posterior distributions for the transport coefficient for amyloid positive and negative groups.

2.3 Posterior predictive simulations

Our cohort contains n = 24 subjects, n = 21 amyloid positive and n = 3 amyloid negative, for which both global tau and atrophy data trajectories exhibit an increasing slope. These subjects align with our model assumptions that tau pathology and tissue atrophy should be increasing in Alzheimer's disease patients.

Figures 7 and 8 show our model predictions for tau and atrophy dynamics in the entorhinal cortex during the first four years after baseline tau positron emission tomography in direct comparison to the observed data. The entorhinal

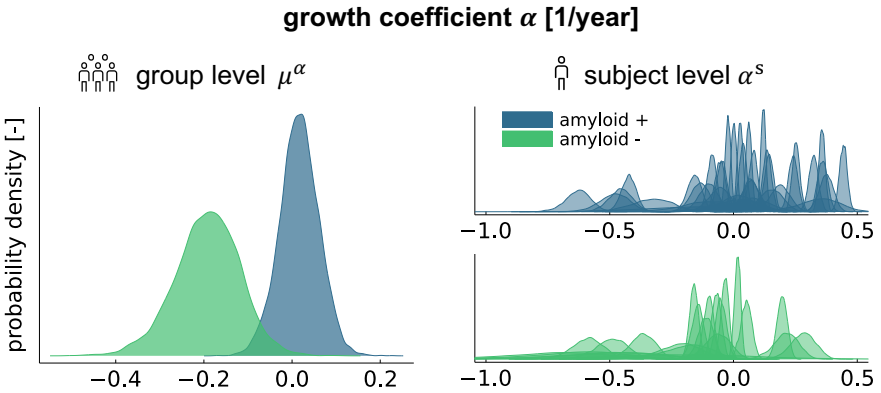

Fig. 5 Posterior distributions. Group- and subject-level posterior distributions for the growth coefficient for amyloid positive and negative groups.

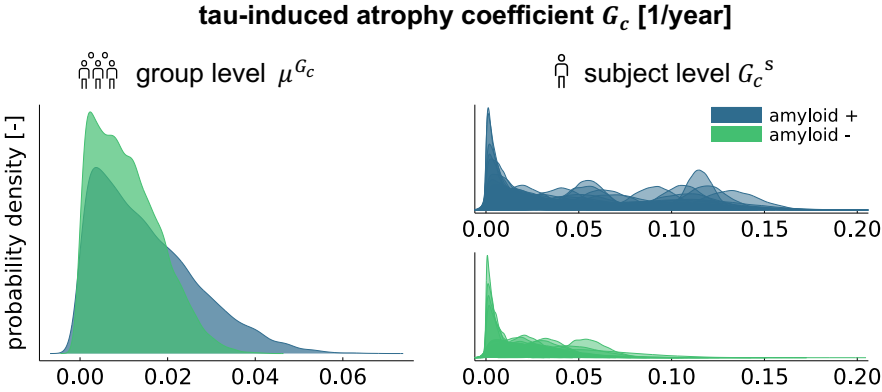

Fig. 6 Posterior distributions. Group- and subject-level posterior distributions for the tau-induced atrophy coefficient for amyloid positive and negative groups.

cortex is one of the first regions affected by Alzheimer's pathology. Overall, the model performs well in capturing the tau and atrophy dynamics in the selected subjects, however, the credible intervals are relatively narrow and do not always capture all data points. There are two possible explanations for this observation: (1) Our model, Equations (5) and (6), produces strictly monotonic trajectories and is therefore not able to describe non-monotonic patient data; (2) Our hierarchical model structure leads to shrinkage, as it allows us to group information across subjects and thereby prevent overfitting to individual subjects.

Posterior summary				
	$A\beta^+$		$A\beta^-$	
Parameter	**mean**	**std**	**mean**	**std**
μ^{ρ}	0.0214	0.0168	0.0287	0.0226
μ^{α}	0.0165	0.0446	-0.1922	0.0737
μ^{G_c}	0.0151	0.0115	0.0108	0.0075

Table 1 Posterior summary. Mean values and standard deviations for model parameter hyperdistributions and noise estimates for tau and atrophy data for amyloid positive and negative groups.

3 Methods

3.1 A coupled network model for tau and atrophy

We describe the spatiotemporal dynamics of tau protein misfolding and propagating across the brain using the classical Fisher-Kolmogorov-Petrovskii-Piskunov model [38] with a source term and a diffusion term,

$$\frac{\mathrm{d}c}{\mathrm{d}t} = \mathrm{div}(\mathbf{K} \cdot \nabla c) + \alpha\, c\,[\,1 - c\,]. \tag{1}$$

Equation (1) characterizes the concentration of misfolded tau protein c scaled between 0 and 1, depending on a diffusion tensor $\mathbf{K}$ that determines the speed and directionality of protein transport and a growth coefficient α that determines how much pathological protein is produced or cleared locally. We assume a one-way coupling between the misfolded tau concentration and brain atrophy of the form

$$\frac{\mathrm{d}q}{\mathrm{d}t} = [\,1 - q\,]\, G_c\, c, \tag{2}$$

where q denotes the local amount of tissue atrophy depending on the local amount of misfolded tau c mitigated by a global tau-induced atrophy coefficient G_c [35].

We solve Equations (1) and (2) on a network model of the brain represented by an undirected graph $G = \{E, N\}$. In this graph, the nodes N describe 83 anatomical regions of interest and the edges E represent neuronal connections between these regions. The connection strength between each pair of nodes is summarized in the weighted adjacency matrix $\mathbf{W}$ with entries W_{ij} informed by diffusion tensor images of $n = 426$ participants of the human connectome project [39]. In line with previous studies [35, 40], we define the weights of the adjacency matrix as $W_{ij} = n_{ij}/\ell_{ij}^2$, where n_{ij} denotes the average number of white matter fibers detected between two regions of interest and ℓ_{ij} denotes the average fiber length along the connection. The files used to create the adjacency matrix are freely available [41, 42] as is the final adjacency matrix [43]. To discretize Equation (1), we use the weighted graph Laplacian

$$\mathbf{L} = \mathbf{D} - \mathbf{W}\,, \tag{3}$$

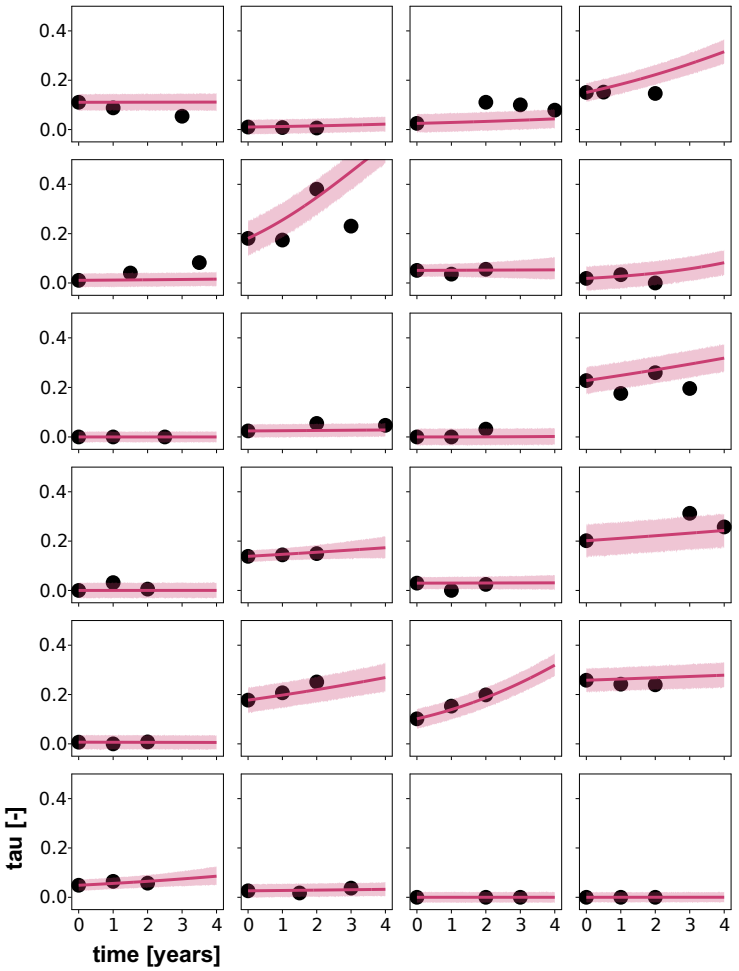

Fig. 7 Posterior predictive simulations. Model predictions for misfolded tau concentration in the entorhinal cortex compared to observed data from longitudinal tau positron emission tomography. Each subplot represents one subject with circles indicating data points, solid red lines showing the median model prediction, and shaded areas representing the 95% credible intervals.

where $\mathbf{D}$ is a diagonal matrix with entries

$$D_{ii} = \sum_{j=1}^{N} W_{ij} \tag{4}$$

This discretization of the diffusion operator preserves both mass and the Fickian property that no transport takes place when two regions have the same concentrations [44]. Then, the discretization of Equation (1) on the brain

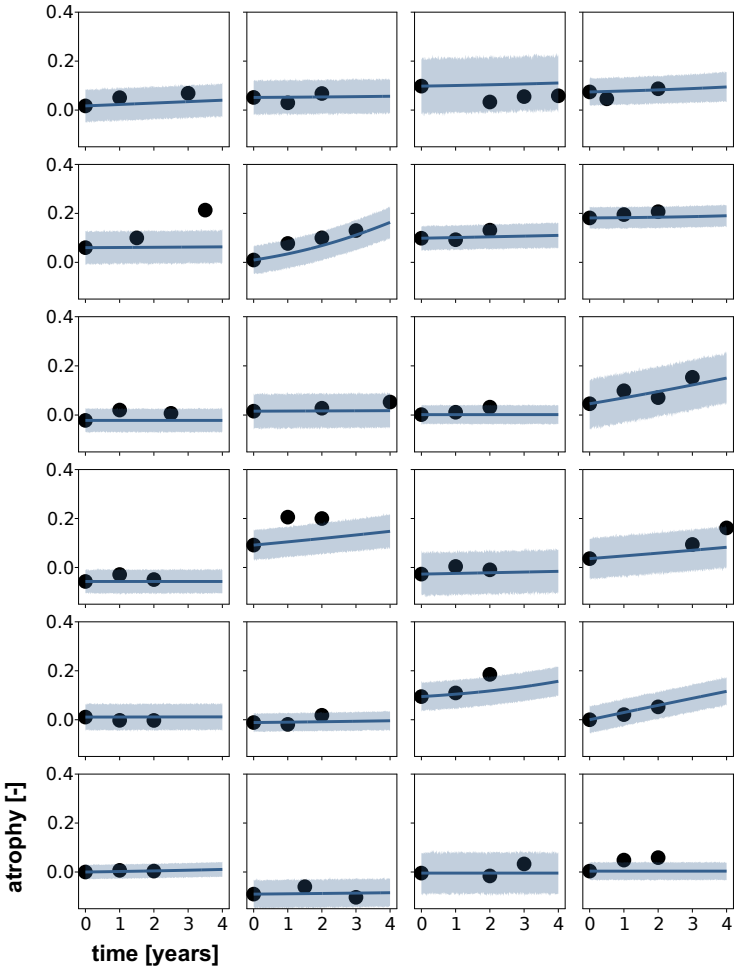

Fig. 8 Posterior predictive simulations. Model predictions for atrophy in the entorhinal cortex compared to observed data from longitudinal structural magnetic resonance imaging. Each subplot represents one subject with circles indicating data points, solid blue lines showing the median model prediction, and shaded areas representing the 95% credible intervals.

network is

$$\frac{\mathrm{d}c_i}{\mathrm{d}t} = -\rho \sum_{j=1}^{N} L_{ij}\, c_j + \alpha\, c_i\,[\,1 - c_i\,], \quad i = 1, \ldots, N \tag{5}$$

with c_i denoting the normalized concentration of toxic tau protein in regions $i = 1, 2, \ldots, N$, ρ acting as a transport coefficient, α as a growth coefficient, and L_{ij} denoting the entries of $\mathbf{L}$. In addition, we define a local measure of

tissue atrophy q_i for each region i

$$\frac{\mathrm{d}q_i}{\mathrm{d}t} = G_c\, c_i[\,1 - q_i\,], \quad i = 1, \ldots, N. \tag{6}$$

in terms of the local tau protein concentration c_i and the tau-induced atrophy coefficient G_c. Combined, the coupled model encompasses three model parameters that can be tuned to match subject-specific disease trajectories: the transport coefficient ρ, the growth rate α, and the tau-induced atrophy coefficient G_c.

3.2 Subject data

We calibrate our coupled tau-atrophy model using longitudinal tau positron emission tomography and structural magnetic resonance data from $n = 61$ subjects of the Alzheimer's Disease Neuroimaging Initiative (ADNI) database [36]. All subjects have undergone between three and five consecutive tau positron emission tomography scans and corresponding structural imaging within six months of the tomography scan. On average, longitudinal scans were separated by 1.15 years. Out of the full set, $n = 38$ subjects were previously identified as amyloid positive and $n = 23$ as amyloid negative [37]. Table 2 summarizes the composition of cognitive diagnoses for the full cohort and each amyloid group.

Demographics				
Amyloid status	**CN**	**SMC**	**MCI**	**total**
positive	n=16	n=9	n=13	n=38
negative	n=8	n=5	n=10	n=23
total	n=24	n=14	n=23	n=61

Table 2 Subject demographics. Demographics by cognitive diagnosis for whole cohort and each amyloid group. Key: CN, cognitively normal; SMC, significant memory concern; MCI, mild cognitive impairment.

3.2.1 Tau data preparation

Tau AV1451-PET data were processed by ADNI according to standard protocols [36, 45]. Each positron emission tomography image was co-registered to a corresponding high-resolution T1 weighted magnetic resonance image and segmented into 68 cortical and 15 subcortical regions according to the Desikan-Killiany atlas [46]. The resulting 83 regions align with the nodes of the brain network described in Section 3.1. After normalizing with respect to the inferior cerebellum, ADNI provides regional standardizes uptake value ratios for all considered subjects and time points. Tau positron emission tomography

measurements in subcortical regions can be contaminated by off-target binding in the choroid plexus and nearby vascular structures [47–49]. Therefore, we base our tau model calibration on the tau positron emission tomography data from cortical regions only. We map the standardized uptake value ratios into a zero-to-one interval following previously described methods [30]. This allows for direct comparison between our model output $\mathbf{c}^{\mathrm{sim}}$ and the data, in the form of a regional normalized tau concentration $0 \leq \mathbf{c}^{\mathrm{pet}} \leq 1$. For each subject, the initial conditions for the protein field of our model are given by the tau uptake values measured in the baseline positron emission tomography scan $\mathbf{c}^{\mathrm{sim}}(t=0) = \mathbf{c}^{\mathrm{pet}}(t_0)$.

3.2.2 Atrophy data preparation

We use Freesurfer [50] in combination with the Clinica [51] t1-freesurfer-longitudinal pipeline to extract regional volume information from the structural magnetic resonance images. For every included subject and visit, we compute volume measures for all 83 brain regions contained in our network model. Many of the subjects included in this study underwent a number of study visits at which only structural image data was obtained, before ADNI started to routinely include tau positron emission tomography. Therefore, we include additional information about regional brain volumes for up to twelve years before the first tau positron emission tomography baseline scan. For each subject, we use the earliest available structural scan to determine regional reference volumes $\mathbf{v}_0^{\mathrm{raw}}$ to which we normalize the regional volumes of all follow-up visits within each subject $\mathbf{v}^{\mathrm{mri}} = \mathbf{v}^{\mathrm{raw}}/\mathbf{v}_0^{\mathrm{raw}}$. We define a measure of nodal atrophy as the relative reduction in volume, $\mathbf{q}^{\mathrm{mri}} = 1 - \mathbf{v}^{\mathrm{mri}}$, with an initial atrophy value at the baseline structural magnetic resonance image of $\mathbf{q}_0^{\mathrm{mri}} = 1 - \mathbf{v}_0^{\mathrm{mri}}$. For each subject, we set the initial conditions for the atrophy field of our model to the relative atrophy values measured at time of the first tau positron emission tomography.

3.3 Bayesian inference

For each subject, we personalize the parameters of our model such that the model predictions best reflect the image data. For inference, we define subject-specific model parameters $\boldsymbol{\vartheta} = \{\, \rho^s, \alpha^s, G_c^s, \sigma_{\mathrm{t}}^{\mathrm{s}}, \sigma_{\mathrm{a}}^{\mathrm{s}} \,\}$ for $s = 1, \ldots, N$ subjects, containing a transport coefficient ρ^{s}, a growth coefficient α^{s}, and a tau-induced atrophy coefficient G_c^{s}. We also use hierarchical priors to group information across subjects, with hyperparameters $\boldsymbol{\varphi} = \{\mu^\rho, \sigma^\rho, \mu^\alpha, \sigma^\alpha, \mu^{G_c}, \sigma^{G_c}\}$. Using this model construction, we compute the posterior distributions for parameters, $\boldsymbol{\vartheta}$ and $\boldsymbol{\varphi}$, given tau PET data, $\mathbf{c}^{\mathrm{pet}}$, and structural MRI atrophy data, $\mathbf{q}^{\mathrm{mri}}$. We calculate the posterior, $p(\boldsymbol{\vartheta}, \boldsymbol{\varphi} | \mathbf{c}^{\mathrm{pet}}, \mathbf{q}^{\mathrm{mri}})$ using Bayes' rule:

$$p(\boldsymbol{\vartheta}, \boldsymbol{\varphi} | \mathbf{c}^{\mathrm{pet}}, \mathbf{q}^{\mathrm{mri}}) = \frac{p(\mathbf{c}^{\mathrm{pet}}, \mathbf{q}^{\mathrm{mri}} | \boldsymbol{\vartheta}, \boldsymbol{\varphi})\; p(\boldsymbol{\vartheta}, \boldsymbol{\varphi})}{p(\mathbf{c}^{\mathrm{pet}}, \mathbf{q}^{\mathrm{mri}})}, \tag{7}$$

Here, $p(\mathbf{c}^{\text{pet}}, \mathbf{q}^{\text{mri}}|\boldsymbol{\vartheta}, \boldsymbol{\varphi})$ denotes the likelihood, $p(\boldsymbol{\vartheta}, \boldsymbol{\varphi})$ are the priors for our parameters and hyperparameters, and $p(\mathbf{c}^{\text{pet}}, \mathbf{q}^{\text{mri}})$ are the evidence.

For the likelihood, we assume a Gaussian error model with independent and identically distributed noise at each PET and structural MRI measurement time,

$$\mathbf{c}^{\text{pet}}_{s,t} \sim \mathcal{N}(\mathbf{c}(\boldsymbol{\vartheta}_s, t), \sigma^{\text{s}}_{\text{t}} I). \tag{8}$$

$$\mathbf{q}^{\text{mri}}_{s,t} \sim \mathcal{N}(\mathbf{q}(\boldsymbol{\vartheta}_s, t), \sigma^{\text{s}}_{\text{a}} I). \tag{9}$$

for $s = 1, \ldots, N$ subjects; $t = 1, \ldots, T_s$, where T_s is the total number of tau PET scans for subject s, $\mathbf{p}(\boldsymbol{\vartheta}_s, t)$ and $\mathbf{q}(\boldsymbol{\vartheta}_s, t)$ are the solutions to the coupled ordinary differential equations (5–6), and $\sigma^{\text{s}}_{\text{t}}$ and $\sigma^{\text{s}}_{\text{a}}$ are the subject-specific standard deviations for the Gaussian error model. We assume the hierarchical structure illustrated in Figure 9 to inform the prior distributions for our model parameters $\boldsymbol{\vartheta}$ and hyperparameters $\boldsymbol{\varphi}$. This approach allows us to gain personalized posterior distributions while simultaneously accounting for commonalities between subjects [52]. Specifically, we propose that the hyperparameters of the subject-specific prior distributions are drawn from one common set of hyperdistributions $\{\mu^{\rho}_{\text{A}\beta+}, \sigma^{\rho}_{\text{A}\beta+}, \mu^{\alpha}_{\text{A}\beta+}, \sigma^{\alpha}_{\text{A}\beta+}, \mu^{G_c}_{\text{A}\beta+}, \sigma^{G_c}_{\text{A}\beta+}\}$ if the subject is amyloid positive, or another common set of hyperdistributions $\{\mu^{\rho}_{\text{A}\beta-}, \sigma^{\rho}_{\text{A}\beta-}, \mu^{\alpha}_{\text{A}\beta-}, \sigma^{\alpha}_{\text{A}\beta-}, \mu^{G_c}_{\text{A}\beta-}, \sigma^{G_c}_{\text{A}\beta-}\}$ if the subject is amyloid negative. This distinction allows us to account for potential differences in tau and atro-

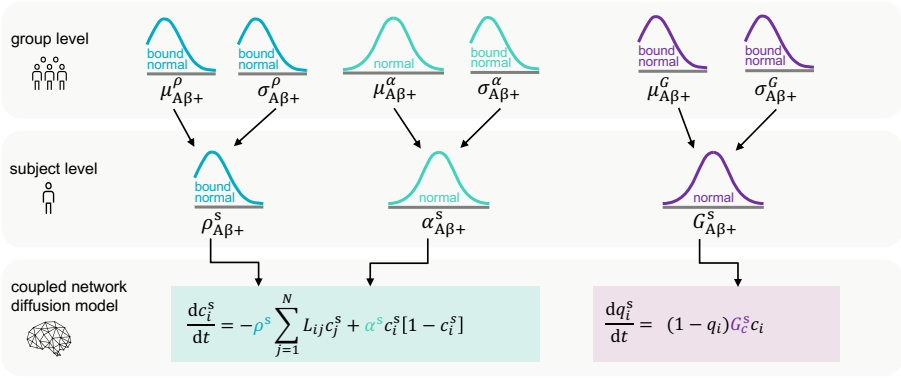

Fig. 9 Hierarchical model. Hierarchical structure for our prior distributions for the amyloid positive subject group. The same prior structure applies to the amyloid negative cohort.

phy dynamics between amyloid groups, as well as likely similarities within amyloid groups. We select informative priors for our hyperparameters $\boldsymbol{\varphi}$ based on previous results [30, 35]. The full list of priors is summarized in Table 3. Note that the priors for both amyloid groups are identical, such that any difference in posteriors will result purely from differences in the data.

Parameter	Prior distribution
$\mu^{\rho}_{\mathrm{A}\beta+/\mathrm{A}\beta-}$	TruncatedNormal($0 < \mu^{\rho} < 3$, mean=0, std=1)
$\sigma^{\rho}_{\mathrm{A}\beta+/\mathrm{A}\beta-}$	TruncatedNormal($0 < \sigma^{\rho} < 3$, mean=0, std=1)
$\rho^{\mathrm{s}}_{\mathrm{A}\beta+/\mathrm{A}\beta-}$	TruncatedNormal($0 < \rho^{\mathrm{s}} < 5$, mean=$\mu^{\rho}$,std=$\sigma^{\rho}$)
$\mu^{\alpha}_{\mathrm{A}\beta+/\mathrm{A}\beta-}$	Normal(mean=0, std=1)
$\sigma^{\alpha}_{\mathrm{A}\beta+/\mathrm{A}\beta-}$	TruncatedNormal($0 < \sigma^{\alpha} < 3$, mean=0, std=1)
$\alpha^{\mathrm{s}}_{\mathrm{A}\beta+/\mathrm{A}\beta-}$	Normal($0 < \alpha^{\mathrm{s}} < 5$, mean=$\mu^{\alpha}$,std=$\sigma^{\alpha}$)
$\mu^{G_c}_{\mathrm{A}\beta+/\mathrm{A}\beta-}$	TruncatedNormal($0 < \mu^{G_c} < 3$, mean=0, std=1)
$\sigma^{G_c}_{\mathrm{A}\beta+/\mathrm{A}\beta-}$	TruncatedNormal($0 < \sigma^{G_c} < 3$, mean=0, std=1)
$G^{\mathrm{s}}_{c,\mathrm{A}\beta+/\mathrm{A}\beta-}$	TruncatedNormal($0 < G^{\mathrm{s}}_{c} < 5$, mean=$\mu^{G_c}$,std=$\sigma^{G_c}$)
$\sigma^{\mathrm{s}}_{\mathrm{t}}$, $\sigma^{\mathrm{s}}_{\mathrm{a}}$	InverseGamma(shape=2, scale=3)

Table 3 Prior distributions. Prior distributions for the personalized model parameters and corresponding hyperparameters, and the noise associated with tau and atrophy data.

We personalize our model with respect to the imaging data by evaluating Equations (7) numerically using two frequently used Julia packages. Specifically, we solve Equations (5) and (6) in time using the DifferentialEquations.jl library [53] and perform inference using the Turing.jl probabilistic programming library [54]. We use the a No-U-Turn-Sampler [55] to sample four chains per subject with 1000 tuning samples and 2000 posterior samples per chain.

After inference, we simulate posterior predictive curves for a subset of subjects. Specifically, we select those subjects for which a linear regression on the globally averaged tau and atrophy data indicates positive slopes for both tau and atrophy dynamics. For these subjects, the data aligns with our model assumptions of increasing tau and atrophy over time, thus we expect optimal conditions for our model performance. We propagate the uncertainty from the personalized posterior parameter distributions through the model to create posterior predictions of global tau and atrophy dynamics, including credible intervals, that can be compared to the observed data.

4 Discussion

In this study, we presented an extension of our previous work to develop a coupled tau-atrophy model informed by clinical observations and personalized its model parameters to multi-modal neuroimaging data of $\mathrm{n} = 61$ subjects. We employed a hierarchical model to perform Bayesian inference, which allowed us to find significant differences between amyloid positive and negative groups for two model parameters, the misfolded tau growth coefficient α and the

tau-induced atrophy coefficient G_c. For the growth coefficient, we identified group-level mean values of 0.0161/year and -0.2042/year for amyloid positive and negative groups, respectively. In the context of the Fisher-Kolmogorov model we chose for describing tau misfolding and propagation, a negative growth rate implies that protein clearance dominates over production. For the atrophy coefficient, we identified group-level mean values of 0.0165/year and 0.0111/year for amyloid positive and negative groups, respectively. These group level differences between amyloid positive and negative subjects *support our hypothesis that the presence of amyloid plaques in the brain has a magnifying influence on tau and atrophy dynamics.* These findings are consistent with other studies observing that the presence of amyloid significantly increases misfolded tau aggregation [56] and tau-induced neuronal loss [57]. We identified a very low transport coefficient independent of amyloid status, consistent with previous findings [30, 58].

When we previously personalized our computational model to a small preliminary data set of n = 4 subjects, we found the tau-induced atrophy coefficient G_c to be in a very similar range for all subjects, despite large variability in tau and atrophy trajectories between subjects. When extending our calibration to a larger cohort of subjects in the current study, we discovered more variability in tau-induced atrophy coefficients, indicating that the relationship between tau pathology and induced neurodegeneration may be fairly complex and entail biological factors that are most likely subject-specific.

Our analysis of the volume data indicates that any current or prospective Alzheimer's patients in the cohort are in very early stages of the disease, when atrophy is mostly pronounced in the basal ganglia regions and parts of the temporal lobe. The atrophy data confirm two main hypotheses: *Atrophy and atrophy rates are more pronounced in amyloid positive than in amyloid negative subjects, and the spatiotemporal progression of atrophy mirrors the known topographic pattern of tau.* The lack of representation of more advanced disease stages in our cohort may prevent us from testing our model performance and predictive capacity on more advanced pathology. However, as more longitudinal scans become available for our subjects, we can naturally address this potential limitation.

The posterior predictive simulations for a subset of n = 24 subjects show overall good performance of the model in capturing the observed data. By design, the model fails to describe tau or atrophy trajectories that are non-monotonic. Our model also performs weakly when there is a small increase in tau pathology but steep increase in atrophy or vice versa. The linear coupling between tau and atrophy through the coefficient G_c in our model fails to reflect scenarios in which tau pathology is increasing slowly and linearly, but atrophy is increasing fast and exponentially. This limitation may be resolved by developing more complex atrophy models that allow for non tau-related avenues of atrophy. We chose a simplistic model here because there is currently not enough longitudinal multi-modal imaging data available to ensure parameter identifiability of more complex models with more parameters during inference.

Limited data availability lead us to make simplifications in our inference methods. For example, we did not include any potential noise in the initial conditions extracted from the baseline images. This simplification reduces the number of parameters to infer and makes our approach a viable compromise between model expressiveness and identifiability.

Naturally, the growing amount of subject data in the future will allow us to improve our procedure and increase statistical certainty in our conclusions. To this end, Bayesian methods are the optimal tool to work with continuously updated data, and explore more complex models and assumptions in the future.

5 Conclusion

This study extends our previous work by personalizing a familiar coupled tau-atrophy model to a larger data set. The model intrinsically captures known features of atrophy including the early acceleration, late deceleration of atrophy rates and the regional heterogeneity of atrophy that closely follows the spatiotemporal pattern of tau neurofibrillary tangle invasion. Extending our data set for model validation to more subjects allows us to confirm our hypothesis that amyloid status affects tau and atrophy dynamics. This is manifested in the distinct group-level posterior distributions for two out of three model parameters. Our Bayesian approach provides personalized model parameters, uncertainties, and model predictions and allows us to characterize the tau- and atrophy-related pathology in single individuals and in groups of amyloid positive and negative subjects. A better understanding of the interplay of amyloid-beta, tau, and atrophy, fueled by the ability to measure these biomarkers in vivo and non-invasively in the living brain, could open doors to advance diagnosis and early treatment in Alzheimer's disease.

Acknowledgments. A. Schaefer was supported by a Brit and Alex d'Arbeloff Stanford Graduate Fellowship to AS. P. Chaggar was supported by funding from the Engineering and Physical Sciences Research Council grant EP/L016044/1 and Roche. A. Goriely was supported by the Engineering and Physical Sciences Research Council grant EP/R020205/1. E. Kuhl was supported by the National Science Foundation grant CMMI 1727268.

Data collection and sharing for this project was funded by the Alzheimer's Disease Neuroimaging Initiative (ADNI) (National Institutes of Health Grant U01 AG024904) and DOD ADNI (Department of Defense award number W81XWH-12-2-0012). ADNI is funded by the National Institute on Aging, the National Institute of Biomedical Imaging and Bioengineering, and through generous contributions from the following: AbbVie, Alzheimer's Association; Alzheimer's Drug Discovery Foundation; Araclon Biotech; BioClinica, Inc.; Biogen; Bristol-Myers Squibb Company; CereSpir, Inc.; Cogstate; Eisai Inc.; Elan Pharmaceuticals, Inc.; Eli Lilly and Company; EuroImmun; F. Hoffmann-La Roche Ltd and its affiliated company Genentech, Inc.; Fujirebio;

GE Healthcare; IXICO Ltd.; Janssen Alzheimer Immunotherapy Research & Development, LLC.; Johnson & Johnson Pharmaceutical Research & Development LLC.; Lumosity; Lundbeck; Merck & Co., Inc.; Meso Scale Diagnostics, LLC.; NeuroRx Research; Neurotrack Technologies; Novartis Pharmaceuticals Corporation; Pfizer Inc.; Piramal Imaging; Servier; Takeda Pharmaceutical Company; and Transition Therapeutics. The Canadian Institutes of Health Research is providing funds to support ADNI clinical sites in Canada. Private sector contributions are facilitated by the Foundation for the National Institutes of Health (www.fnih.org). The grantee organization is the Northern California Institute for Research and Education, and the study is coordinated by the Alzheimer's Therapeutic Research Institute at the University of Southern California. ADNI data are disseminated by the Laboratory for Neuro Imaging at the University of Southern California.

References

[1] Alzheimer, A.: über eine eigenartige Erkrankung der Hirnrinde. Zentralbl. Nervenh. Psych. **18**, 177–179 (1907)

[2] Villemagne, V.L., Doré, V., Burnham, S.C., Masters, C.L., Rowe, C.C.: Imaging tau and amyloid-β proteinopathies in Alzheimer disease and other conditions. Nature Reviews Neurology **14**(4), 225–236 (2018)

[3] Johnson, K.A., Schultz, A., Betensky, R.A., Becker, J.A., Sepulcre, J., Rentz, D., Mormino, E., Chhatwal, J., Amariglio, R., Papp, K., *et al.*: Tau positron emission tomographic imaging in aging and early Alzheimer disease. Annals of neurology **79**(1), 110–119 (2016)

[4] Selkoe, D.J., Hardy, J.: The amyloid hypothesis of Alzheimer's disease at 25 years. EMBO molecular medicine **8**(6), 595–608 (2016)

[5] Bejanin, A., Schonhaut, D.R., La Joie, R., Kramer, J.H., Baker, S.L., Sosa, N., Ayakta, N., Cantwell, A., Janabi, M., Lauriola, M., *et al.*: Tau pathology and neurodegeneration contribute to cognitive impairment in Alzheimer's disease. Brain **140**(12), 3286–3300 (2017)

[6] Ossenkoppele, R., Schonhaut, D.R., Schöll, M., Lockhart, S.N., Ayakta, N., Baker, S.L., O'Neil, J.P., Janabi, M., Lazaris, A., Cantwell, A., *et al.*: Tau PET patterns mirror clinical and neuroanatomical variability in Alzheimer's disease. Brain **139**(5), 1551–1567 (2016)

[7] Harrison, T.M., La Joie, R., Maass, A., Baker, S.L., Swinnerton, K., Fenton, L., Mellinger, T.J., Edwards, L., Pham, J., Miller, B.L., *et al.*: Longitudinal tau accumulation and atrophy in aging and Alzheimer disease. Annals of Neurology **85**(2), 229–240 (2019)

[8] La Joie, R., Visani, A.V., Baker, S.L., Brown, J.A., Bourakova, V.,

Cha, J., Chaudhary, K., Edwards, L., Iaccarino, L., Janabi, M., et al.: Prospective longitudinal atrophy in Alzheimer's disease correlates with the intensity and topography of baseline tau-PET. Science translational medicine **12**(524) (2020)

[9] Xia, C., Makaretz, S.J., Caso, C., McGinnis, S., Gomperts, S.N., Sepulcre, J., Gomez-Isla, T., Hyman, B.T., Schultz, A., Vasdev, N., *et al.*: Association of in vivo [18F] AV-1451 tau PET imaging results with cortical atrophy and symptoms in typical and atypical Alzheimer disease. JAMA neurology **74**(4), 427–436 (2017)

[10] Bobinski, M., De Leon, M., Wegiel, J., Desanti, S., Convit, A., Saint Louis, L., Rusinek, H., Wisniewski, H.: The histological validation of post mortem magnetic resonance imaging-determined hippocampal volume in Alzheimer's disease. Neuroscience **95**(3), 721–725 (1999)

[11] Dickerson, B.C., Bakkour, A., Salat, D.H., Feczko, E., Pacheco, J., Greve, D.N., Grodstein, F., Wright, C.I., Blacker, D., Rosas, H.D., *et al.*: The cortical signature of Alzheimer's disease: regionally specific cortical thinning relates to symptom severity in very mild to mild AD dementia and is detectable in asymptomatic amyloid-positive individuals. Cerebral cortex **19**(3), 497–510 (2009)

[12] Pini, L., Pievani, M., Bocchetta, M., Altomare, D., Bosco, P., Cavedo, E., Galluzzi, S., Marizzoni, M., Frisoni, G.B.: Brain atrophy in Alzheimer's disease and aging. Ageing research reviews **30**, 25–48 (2016)

[13] Nestor, S.M., Rupsingh, R., Borrie, M., Smith, M., Accomazzi, V., Wells, J.L., Fogarty, J., Bartha, R., Initiative, A.D.N.: Ventricular enlargement as a possible measure of Alzheimer's disease progression validated using the Alzheimer's disease neuroimaging initiative database. Brain **131**(9), 2443–2454 (2008)

[14] Sabuncu, M.R., Desikan, R.S., Sepulcre, J., Yeo, B.T.T., Liu, H., Schmansky, N.J., Reuter, M., Weiner, M.W., Buckner, R.L., Sperling, R.A., *et al.*: The dynamics of cortical and hippocampal atrophy in Alzheimer disease. Archives of neurology **68**(8), 1040–1048 (2011)

[15] Fox, N.C., Freeborough, P.A.: Brain atrophy progression measured from registered serial MRI: validation and application to Alzheimer's disease. Journal of Magnetic Resonance Imaging **7**(6), 1069–1075 (1997)

[16] Ridha, B.H., Barnes, J., Bartlett, J.W., Godbolt, A., Pepple, T., Rossor, M.N., Fox, N.C.: Tracking atrophy progression in familial Alzheimer's disease: a serial MRI study. The Lancet Neurology **5**(10), 828–834 (2006)

[17] Jack, C., Weigand, S.D., Shiung, M.M., Przybelski, S.A., O'Brien, P.C.,

Gunter, J.L., Knopman, D.S., Boeve, B.F., Smith, G.E., Petersen, R.C.: Atrophy rates accelerate in amnestic mild cognitive impairment. Neurology **70**(19 Part 2), 1740–1752 (2008)

[18] Henneman, W., Sluimer, J., Barnes, J., Van Der Flier, W., Sluimer, I., Fox, N., Scheltens, P., Vrenken, H., Barkhof, F.: Hippocampal atrophy rates in Alzheimer disease: added value over whole brain volume measures. Neurology **72**(11), 999–1007 (2009)

[19] Sluimer, J.D., van der Flier, W.M., Karas, G.B., van Schijndel, R., Barnes, J., Boyes, R.G., Cover, K.S., Olabarriaga, S.D., Fox, N.C., Scheltens, P., *et al.*: Accelerating regional atrophy rates in the progression from normal aging to Alzheimer's disease. European radiology **19**(12), 2826–2833 (2009)

[20] McDonald, C., McEvoy, L., Gharapetian, L., Fennema-Notestine, C., Hagler, D., Holland, D., Koyama, A., Brewer, J., Dale, A., *et al.*: Regional rates of neocortical atrophy from normal aging to early Alzheimer disease. Neurology **73**(6), 457–465 (2009)

[21] Josephs, K.A., Martin, P.R., Weigand, S.D., Tosakulwong, N., Buciuc, M., Murray, M.E., Petrucelli, L., Senjem, M.L., Spychalla, A.J., Knopman, D.S., *et al.*: Protein contributions to brain atrophy acceleration in Alzheimer's disease and primary age-related tauopathy. Brain **143**(11), 3463–3476 (2020)

[22] Das, S.R., Xie, L., Wisse, L.E., Ittyerah, R., Tustison, N.J., Dickerson, B.C., Yushkevich, P.A., Wolk, D.A., Initiative, A.D.N., *et al.*: Longitudinal and cross-sectional structural magnetic resonance imaging correlates of AV-1451 uptake. Neurobiology of aging **66**, 49–58 (2018)

[23] Thompson, P.M., Hayashi, K.M., De Zubicaray, G., Janke, A.L., Rose, S.E., Semple, J., Herman, D., Hong, M.S., Dittmer, S.S., Doddrell, D.M., *et al.*: Dynamics of gray matter loss in Alzheimer's disease. Journal of neuroscience **23**(3), 994–1005 (2003)

[24] Frisoni, G.B., Prestia, A., Rasser, P.E., Bonetti, M., Thompson, P.M.: In vivo mapping of incremental cortical atrophy from incipient to overt Alzheimer's disease. Journal of neurology **256**(6), 916–924 (2009)

[25] Singh, V., Chertkow, H., Lerch, J.P., Evans, A.C., Dorr, A.E., Kabani, N.J.: Spatial patterns of cortical thinning in mild cognitive impairment and Alzheimer's disease. Brain **129**(11), 2885–2893 (2006)

[26] Jack Jr, C.R., Barkhof, F., Bernstein, M.A., Cantillon, M., Cole, P.E., DeCarli, C., Dubois, B., Duchesne, S., Fox, N.C., Frisoni, G.B., *et al.*: Steps to standardization and validation of hippocampal volumetry as a

biomarker in clinical trials and diagnostic criterion for Alzheimer's disease. Alzheimer's & Dementia **7**(4), 474–485 (2011)

[27] Vogel, J., Iturria-Medina, Y., Hansson, O., *et al.*: Four distinct trajectories of tau deposition identified in Alzheimer's disease. Nat. Commun. **27**, 871–881 (2021)

[28] Raj, A., Kuceyeski, A., Weiner, M.: A network diffusion model of disease progression in dementia. Neuron **73**(6), 1204–1215 (2012)

[29] Torok, J., Maia, P.D., Powell, F., Pandya, S., Raj, A.: A method for inferring regional origins of neurodegeneration. Brain **141**(3), 863–876 (2018)

[30] Schäfer, A., Peirlinck, M., Linka, K., Kuhl, E., (ADNI, A.D.N.I., et al.: Bayesian Physics-Based Modeling of Tau Propagation in Alzheimer's Disease. Frontiers in physiology, 1081 (2021)

[31] Weickenmeier, J., Kuhl, E., Goriely, A.: Multiphysics of prionlike diseases: Progression and atrophy. Physical review letters **121**(15), 158101 (2018)

[32] Schäfer, A., Weickenmeier, J., Kuhl, E.: The interplay of biochemical and biomechanical degeneration in Alzheimer's disease. Comput. Methods Appl. Mech. Engrg. **352**, 369–388 (2019)

[33] Raj, A., LoCastro, E., Weiner, M., *et al.*: Network diffusion model of progression predicts longitudinal patterns of atrophy and metabolism in Alzheimer's disease. Cell reports **10**(3), 359–369 (2015)

[34] Blinkouskaya, Y., Weickenmeier, J.: Brain Shape Changes Associated With Cerebral Atrophy in Healthy Aging and Alzheimer's Disease. Frontiers in Mechanical Engineering, 64 (2021)

[35] Schäfer, A., Chaggar, P., Thompson, T.B., Goriely, A., Kuhl, E., Initiative, A.D.N., *et al.*: Predicting brain atrophy from tau pathology: A summary of clinical findings and their translation into personalized models. Brain Multiphysics **2**, 100039 (2021)

[36] ADNI: Alzheimer's Disease Neuroimaging Initiative. (accessed July 31, 2020). http://adni.loni.usc.edu

[37] Landau, S.M., Lu, M., Joshi, A.D., Pontecorvo, M., Mintun, M.A., Trojanowski, J.Q., Shaw, L.M., Jagust, W.J., Initiative, A.D.N.: Comparing positron emission tomography imaging and cerebrospinal fluid measurements of β-amyloid. Annals of Neurology **74**(6), 826–836 (2013)

[38] Kolmogorov, A., Petrovskii, I., Piskunov, N.: A study of the equation of

diffusion with increase in the quantity of matter, and its application to a biological problem. Byul. Moskovskogo Gos. Univ **1**(6), 1–25 (1937)

[39] McNab, J.A., Edlow, B.L., Witzel, T., Huang, S.Y., Bhat, H., Heberlein, K., Feiweier, T., Liu, K., Keil, B., Cohen-Adad, J., *et al.*: The Human Connectome Project and beyond: initial applications of 300 mT/m gradients. Neuroimage **80**, 234–245 (2013)

[40] Thompson, T.B., Chaggar, P., Kuhl, E., Goriely, A.: Protein-protein interactions in neurodegenerative diseases: a conspiracy theory. PLoS Comp. Biol. **16**(10), 1008267 (2020). https://doi.org/10.1371/journal.pcbi.1008267

[41] Kerepesi, C., Szalkai, B., Varga, B.e.a.: The braingraph.org database of high resolution structural connectomes and the brain graph tools. Cogn. Neurodyn. **11**, 483–486 (2017). https://doi.org/10.1007/s11571-017-9445-1

[42] The PIT Bioinformatics group: Connectomes: The Braingraph.org public website. Braingraph.org (2019). https://braingraph.org/cms/download-pit-group-connectomes/

[43] Putra, P., Chaggar, P., Thompson, T., Goriely, A.: Oxford Mathematical Brain Modelling group: Braid surface Matlab source code and master connectome graphs. Github (2021). https://github.com/OxMBM/Connectome-Staging

[44] Putra, P., Thompson, T.B., Chaggar, P., Goriely, A., Initiative, A.D.N., Initiative, A.D.N., et al.: Braiding Braak and Braak: Staging patterns and model selection in network neurodegeneration. Network Neuroscience, 1–41 (2021)

[45] Baker, S.L., *et al.*: Reference Tissue-Based Kinetic Evaluation of 18F-AV1451 for Tau Imaging. J. Nucl. Med. **58**(2), 332–338 (2017)

[46] Desikan, R.S., Ségonne, F., Fischl, B., Quinn, B.T., Dickerson, B.C., Blacker, D., Buckner, R.L., Dale, A.M., Maguire, R.P., Hyman, B.T., *et al.*: An automated labeling system for subdividing the human cerebral cortex on MRI scans into gyral based regions of interest. Neuroimage **31**(3), 968–980 (2006)

[47] Lemoine, L., Leuzy, A., Chiotis, K., Rodriguez-Vieitez, E., Nordberg, A.: Tau positron emission tomography imaging in tauopathies: the added hurdle of off-target binding. Alzheimer's & Dementia: Diagnosis, Assessment & Disease Monitoring **10**, 232–236 (2018)

[48] Marquié, M., Normandin, M.D., Meltzer, A.C., Siao Tick Chong,

M., Andrea, N.V., Antón-Fernández, A., Klunk, W.E., Mathis, C.A., Ikonomovic, M.D., Debnath, M., *et al.*: Pathological correlations of [F-18]-AV-1451 imaging in non-Alzheimer tauopathies. Annals of Neurology **81**(1), 117–128 (2017)

[49] Lowe, V.J., Curran, G., Fang, P., Liesinger, A.M., Josephs, K.A., Parisi, J.E., Kantarci, K., Boeve, B.F., Pandey, M.K., Bruinsma, T., *et al.*: An autoradiographic evaluation of AV-1451 Tau PET in dementia. Acta Neuropathologica Communications **4**(1), 58 (2016)

[50] FreeSurfer: FreeSurfer Software Suite. (accessed July 31, 2020). http://surfer.nmr.mgh.harvard.edu

[51] Routier, A., Burgos, N., Díaz, M., Bacci, M., Bottani, S., El-Rifai, O., Fontanella, S., Gori, P., Guillon, J., Guyot, A., et al.: Clinica: An Open-Source Software Platform for Reproducible Clinical Neuroscience Studies. Frontiers in Neuroinformatics **15** (2021)

[52] Gelman, A., Hill, J.: Data Analysis Using Regression and Multilevel/hierarchical Models. Cambridge university press, Cambridge (2006)

[53] Rackauckas, C., Nie, Q.: Differentialequations.jl–a performant and feature-rich ecosystem for solving differential equations in julia. Journal of Open Research Software **5**(1) (2017)

[54] Ge, H., Xu, K., Ghahramani, Z.: Turing: a language for flexible probabilistic inference. In: International Conference on Artificial Intelligence and Statistics, AISTATS 2018, 9-11 April 2018, Playa Blanca, Lanzarote, Canary Islands, Spain, pp. 1682–1690 (2018). http://proceedings.mlr.press/v84/ge18b.html

[55] Homan, M.D., Gelman, A.: The No-U-Turn Sampler: Adaptively setting path lengths in Hamiltonian Monte Carlo. J. Mach. Learn. Res. **15**(1), 1593–1623 (2014)

[56] Bennett, R.E., DeVos, S.L., Dujardin, S., Corjuc, B., Gor, R., Gonzalez, J., Roe, A.D., Frosch, M.P., Pitstick, R., Carlson, G.A., *et al.*: Enhanced tau aggregation in the presence of amyloid β. The American journal of pathology **187**(7), 1601–1612 (2017)

[57] Pooler, A.M., Hyman, B.T.e.a.: Amyloid accelerates tau propagation and toxicity in a model of early Alzheimer's disease. Acta Neuropathologica Communications **3**(1), 14 (2015). https://doi.org/10.1186/s40478-015-0199-x

[58] Meisl, G., Hidari, E., Allinson, K., Rittman, T., DeVos, S.L., Sanchez,

J.S., Xu, C.K., Duff, K.E., Johnson, K.A., Rowe, J.B., *et al.*: In vivo rate-determining steps of tau seed accumulation in alzheimer's disease. Science advances **7**(44), 1448 (2021)